Article

Research on the Population Flow and Mixing Characteristics of Pelleted Vegetable Seeds Based on the Bonded-Particle Model

Jian Xu [1], Shunli Sun [2], Xiaoting Li [1], Zhiheng Zeng [2], Chongyang Han [2], Ting Tang [2] and Weibin Wu [2,*]

[1] National Navel Orange Engineering Research Centre, College of Life Sciences, Gannan Normal University, Ganzhou 341000, China; xujian@gnnu.edu.cn (J.X.); lixiaoting@gnnu.edu.cn (X.L.)

[2] College of Engineering, South China Agricultural University, Guangzhou 510642, China; sunshunli@stu.scau.edu.cn (S.S.); zengzhiheng@stu.scau.edu.cn (Z.Z.); 20202009003@stu.scau.edu.cn (C.H.); 20203163056@stu.scau.edu.cn (T.T.)

[*] Correspondence: wuweibin@scau.edu.cn

Abstract: In order to precisely reproduce the precise seeding process of the population in the air-suction seed-metering device, it is necessary to execute accurate modeling of seed particles using the bonded-particle model, in combination with the discrete element method (DEM) and computational fluid dynamics (CFD). Through the repose angle, slope screening, rotating container, and particle sedimentation experiments, in this paper, the influence of the filling accuracy of the bonded-particle model on the flow behavior and mixing characteristics of the seed population was first explored based on EDEM software. The viability of the suggested modeling approach for pelleted vegetable seeds, as described in this study, was confirmed by comparing experimental and simulation outcomes. The surface roughness values obtained from the studies above were utilized to assess the accuracy of the bonded-particle model in filling. Additionally, a mathematical technique for determining the surface roughness was provided. Furthermore, an analysis of the multiple contacts in the bonded-particle model was also performed. The results indicated that the simulation results closely matched the experimental data when the number of sub-spheres in the bonded-particle model was equal to or more than 70, as measured by the standard deviation. In addition, the most optimal modeling scheme for the pelletized vegetable seed bonded-particles, based on the cost of coupling simulation, was found to be the bonded-particle surface roughness (BS) with a value of 0.1. Ultimately, a practical example was utilized to demonstrate the utilization of the pelleted vegetable seed bonded-particle model and the DEM-CFD coupling approach in analyzing the accuracy of the seeding process in the air-suction seed-metering device. This example will serve as a valuable reference point for future field studies.

Keywords: computational fluid dynamics; bonded-particle model; discrete element method; pelleted vegetable seeds

1. Introduction

The relationship between pelleted vegetable seeds and mechanical components is crucial for precise planting, seed sorting, and storage in precision agriculture. Historically, experimental methods were used to assess this relationship, resulting in lengthy optimization cycles, expensive processes, and limitations based on the time of year. Furthermore, these techniques frequently miss essential microscopic information, such as particle movement and velocity, which is needed for accurate mechanical design. Nevertheless, this approach is linked to a protracted process of refining and perfecting the design, substantial expenses, and limitations based on the time of year. Furthermore, the experimental approach cannot acquire crucial information such as particle movement, velocity, the force exerted between particles, and contact surface details. These pieces of information are vital for the optimal design of mechanical structures connected to the experiment. Consequently,

Cundall devised a discrete element method (DEM) to accurately forecast the interaction between particles and mechanical components and the movement of particles following a collision [1].

However, besides the contact between particles and mechanical parts, there is also the interaction between fluid and particles in some agricultural engineering fields (pneumatic precision seeding, pneumatic picking, etc.). Agricultural engineering currently extensively uses the coupling of computational fluid dynamics (CFD) and DEM to simulate fluid–solid two-phase flow. The approach can readily account for the parameters of particulate substances and acquire microscopic data regarding particle size [2,3].

When analyzing the interaction between seed particles and their associated mechanical components using computational fluid dynamics and the discrete element method, the precision of the seed particle model becomes critical. When examining the pneumatic precision seeding process of pelleted vegetable seeds, for instance, it is frequently necessary to employ a more accurate seed particle model. Particle and fluid domain grid relative sizes are critical for ensuring accurate coupling during the DEM-CFD coupling process. The method can be divided into analytical and non-analytical CFD-DEM coupling calculation methods based on the relative relationship between particle volume and fluid domain grid volume. The particle volume is considerably greater than the volume of the fluid domain grid in the analytical CFD-DEM coupling calculation method (a single particle can encompass numerous fluid domain grids). Calculating particle-scale microscopic information is a common application of the immersed boundary method (IBM). By employing direct numerical integration, the method is capable of precisely determining the force of the fluid operating on each particle and analyzing the flow field surrounding each particle [4,5]. Mao employed the IBM method to ascertain the interaction force between fluid and solid within various contexts [6]. In addition, Zhao investigated four discrete IBM imposition methodologies in order to simulate gas–solid flows within cylindrical and immersed fluidized beds, single-phase flow within a stationary cylinder, and single-phase conduit flow. In conducting these inquiries, the developers of the CFD-DEM-IBM solver sought to assess its accuracy and effectiveness [7]. Nevertheless, the IBM-based analytical CFD-DEM coupling calculation approach is expensive. At present, the majority of research is devoted to single particles or a small number of particles, which restricts the examination of the fluid–solid coupling characteristics of multiple particles in the agricultural domain [8,9].

In the non-analytical CFD-DEM coupling calculation method, the particle volume is significantly smaller than the fluid domain grid volume (a fluid domain grid can contain many particles). This method cannot precisely solve the flow field around each particle but can model the fluid–particle interaction in the locally averaged flow field grid based on the drag model [10]. Lei employed non-analytical CFD-DEM to simulate the centralized pneumatic seeding system and optimized the critical design features of the seed-metering device, considering the mechanical properties of the seeds within the airflow field [11]. Furthermore, Huang utilized the non-analytical CFD-DEM to simulate the motion trajectory of vegetable seeds within the separation chamber of the wind screening machine. Through this simulation, Huang established a correlation between the operational parameters of the wind screening machine and its cleansing performance [12]. Li additionally utilized the non-analytical CFD-DEM to conduct a gas–solid coupling numerical simulation on the seeds in the seed conveying conduit as a function of varying wind speeds and sowing amounts. This simulation confirmed the viability of coupling simulation as a method for determining the velocity of the seeds [13].

The aforementioned studies developed particle models whose volumes were less than those of the fluid domain grid. Nevertheless, the meticulous meshing of the fluid domain becomes imperative in numerous agricultural engineering scenarios that involve two-phase flows characterized by high flow velocities. Analytical CFD-DEM coupling calculation is, therefore, inappropriate in the majority of situations. At present, when the non-analytical CFD-DEM coupling calculation technique yields a considerably smaller local grid volume in the fluid domain than the particle volume, the majority of studies

employ the particle modeling method based on the bonded-particle model. A collection of sub-particles held together by parallel bonding composes the seed particles. The bonded-particle model conceptualizes a particle as a polymer consisting of a predetermined quantity of sub-particles.

Liu developed a bonded-particle model specifically for corn seeds. The researchers employed this model, in conjunction with the DEM-CFD coupling technique, to replicate and examine the operational procedure of the pneumatic seed-metering system, thereby enhancing its crucial structural characteristics [14]. Han also utilized the bonded-particle method for seed modeling and used EDEM–Fluent to simulate the interaction of gas and solid phases in a maize precision seed-metering mechanism that fills from the inside and uses air blowing. Analyzing the mechanical characteristic parameters of seeds within the airflow field allowed for the optimization of the suction-hole size in the seed-metering mechanism [15]. However, the above research failed to consider the influence of the number of sub-spheres that make up bonded particles (which directly influences the precision of the bonded-particle model) on DEM-CFD simulation calculations. Due to the presence of numerous contacts in the bonded-particle model, collisions result in excessive stiffness and damping. As a result, the behavior of population flow and mixing characteristics undergo considerable changes, making it challenging to match the specific requirements of actual research. Hence, it is necessary to investigate how to create a bonded-particle model that accurately represents the population flow behavior and mixing characteristics when the non-analytical CFD-DEM coupling calculation method has a much smaller local grid volume in the fluid domain compared with the particle volume. Additionally, it is important to examine how changes in the accuracy of the bonded-particle model affect the precision of various simulation tests.

This paper focuses on addressing the aforementioned issues by studying pelleted vegetable seeds and employing the bound particle model to develop a seed population model. The flow behavior and mixing characteristics of the population were analyzed by comparing simulation results of repose angles, slope screening, and rotating containers with experimental results. This analysis also verified the feasibility and effectiveness of the seed bonded-particle model proposed in this paper. Concurrently, an examination was conducted on the precision of various bonded-particle models and their impact on simulation accuracy. Additionally, the cost and accuracy of gas–solid coupling calculations were thoroughly evaluated. The purpose of this analysis was to offer guidance in selecting bonded-particle models that possess suitable levels of accuracy. Ultimately, a practical scenario was utilized to demonstrate the utilization of the pelleted vegetable seed bonded-particle model and DEM-CFD coupling (EDEM 2020 and Fluent 2020) approach in analyzing the accuracy of the seeding process in an air-suction seed-metering equipment. This will serve as a valuable point of reference for future study in this field.

2. Numerical Method

2.1. Particle Modeling Method

In the bonded-particle model, each particle is conceptualized as a polymer comprising a specific number of sub-particles interconnected by cohesive bonds (Figure 1a). An overlap occurs on the circular contact surface when bonding occurs between sub-particles, resulting in tangential moment, normal moment, tangential stress, and normal stress (Figure 1b) [16,17]. The *i* and *j* particles separate if the external force is greater than any critical moment or critical stress, thus breaking the particles.
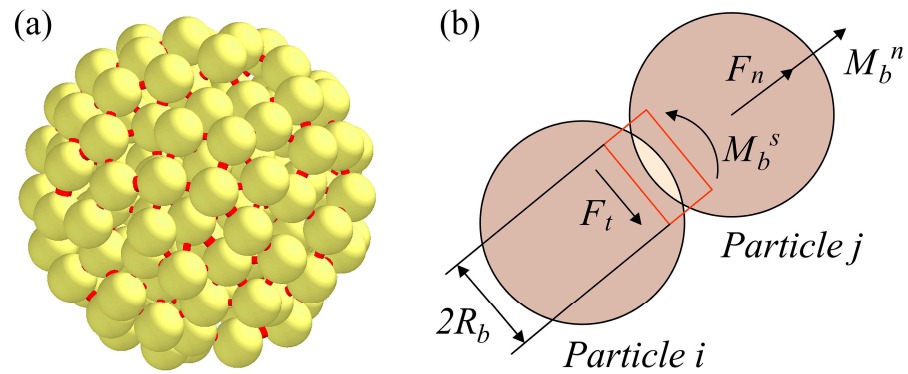
Figure 1. Particle modeling method. (**a**) Bonded-particle model, (**b**) bonding between sub-particles.

At each simulation step, the bonding forces and moment increments between sub-particles are calculated and then resolved into their normal and tangential components relative to the contact plane using Formula (1). The resultant values of force $\left(\vec{F_n}, \vec{F_t} \right)$ and moment $\left(M_b^n, M_b^s \right)$ are determined by adding these increments to their respective values from the previous iteration in the calculation update.

$$
\begin{cases}
\delta \vec{F_n} = -\vec{v_n} k_n A \delta_t \\
\delta \vec{F_t} = -\vec{v_t} k_t A \delta_t \\
\delta M_b^n = -\omega_n k_n J \delta_t \\
\delta M_b^s = -\frac{1}{2} \omega_t k_t J \delta_t
\end{cases}
\tag{1}
$$

Specifically, $\delta \vec{F_n}$ and $\delta \vec{F_n}$ represent the increments of normal and tangential bonding forces, respectively, N; δM_b^n and δM_b^s represent the increments of normal and tangential bonding moment, respectively, N·m; k_n and k_t represent the normal and tangential stiffness, respectively, N/m; $\vec{v_n}$ and $\vec{v_t}$ represent the normal and tangential relative velocity between particles, respectively, m/s. ω_n and ω_t represent the normal and tangential angular velocity, respectively, rad/s. Additionally, δ_t represents the time step, s; A denotes the cross-sectional area of parallel cohesive bond, m^2; J represents the moment of inertia of particles, kg·m.

The bonded-particle model combines particles via virtual cohesive bonds. The cohesive bonds exhibit resilience against minor displacements in both tangential and normal directions until they encounter the thresholds of maximum normal stress $\left(\vec{\sigma}_{max} \right)$ and tangential stress $\left(\vec{\tau}_{max} \right)$. The cohesive bond undergoes fracture either when the maximum normal stress surpasses the critical normal stress (σ_c) or when the maximum tangential stress exceeds the critical tangential stress (τ_c). These stresses can be calculated as follows:

$$
\begin{cases}
\left| \vec{\sigma}_{max} \right| = \left| \frac{\vec{F_n}}{A} + \frac{2 M_b^n}{J} R_b \right| < \sigma_c \\
\left| \vec{\tau}_{max} \right| = \left| \frac{\vec{F_t}}{A} + \frac{2 M_b^s}{J} R_b \right| < \tau_c
\end{cases}
\tag{2}
$$

where R_b is the radius of cohesive bond, m.

The Hertz–Mindlin no-slip model serves as a viable option for defining the contact force interaction between particles and contact materials [18,19]. In the model, the normal component is represented by a non-linearly damped Hertzian spring, wherein the normal contact force F_n is determined by the combined effects of the normal spring force and the normal damping force, as follows:

$$
F_n = k_n \delta_n^{3/2} + c_n \delta_n^{1/4} v_n^{rel}
\tag{3}
$$

where c_n represents the normal damping coefficient; δ_n represents the normal overlap between two contact particles, m; and v_n^{rel} indicates the normal relative velocity between two particles, m/s.

The tangential contact force F_t of Hertz–Mindlin equals the normal contact force F_n. The tangential contact force is calculated as follows:

$$F_t = \min\left\{k_t\delta_n^{1/2}\delta_t + c_t\delta_n^{1/4}v_t^{rel}, \mu_s|F_n|\right\} \tag{4}$$

where c_t represents the tangential damping coefficient; δ_t represents the tangential overlap between two contact particles, m; v_t^{rel} represents the tangential relative velocity between contact particles, m/s; μ_s represents the coefficient of static friction. The spring stiffness and damping coefficients are outlined in Table 1.

Table 1. Spring stiffness and damping coefficients.

	Normal Component	**Tangential Component**
Spring stiffness	$k_n = \frac{4}{3}E^*\sqrt{R^*}$	$k_t = 8G^*\sqrt{R^*}$
Damping coefficient	$c_n = \frac{\ln e}{\sqrt{\ln^2 e + \pi^2}}\sqrt{5m^*k_n}$	$c_t = \frac{\ln e}{\sqrt{\ln^2 e + \pi^2}}\sqrt{\frac{10}{3}m^*k_t}$

Notes: E^* represents the equivalent Young's modulus (Pa), $\frac{1}{E^*} = \frac{(1-v_i^2)}{E_i} + \frac{(1-v_j^2)}{E_j}$; E_i, E_j are Young's moduli of the contacting elements, Pa; e represents the normal restitution coefficient; R^* represents the equivalent radius (m), $\frac{1}{R^*} = \frac{1}{R_i} + \frac{1}{R_j}$; R_i, R_j represent the contacting elements radii, m; m^* represents the equivalent mass (kg), $\frac{1}{m^*} = \frac{1}{m_i} + \frac{1}{m_j}$; m_i, m_j represent the contacting elements masses, kg; G^* represents the equivalent shear modulus (Pa), $\frac{1}{G^*} = \frac{(2-v_i)}{G_i} + \frac{(2-v_j)}{G_j}$; G_i, G_j represent the shear moduli of the contacting elements, Pa; v_i, v_j represent the Poisson's ratio of the contacting elements.

2.2. DEM-CFD Drag Force Model

The drag force of particles in the CFD domain represents the interaction between particles and fluid. Momentum transfer occurs when there is relative motion between fluid and particles. The drag force model is calculated as follows: First, the solid volume fraction in each grid element in the fluid domain is calculated. Briefly, sample points are regularly extracted from the boundary box of the particles and then saved if they are within the boundary of the particles (Figure 2).
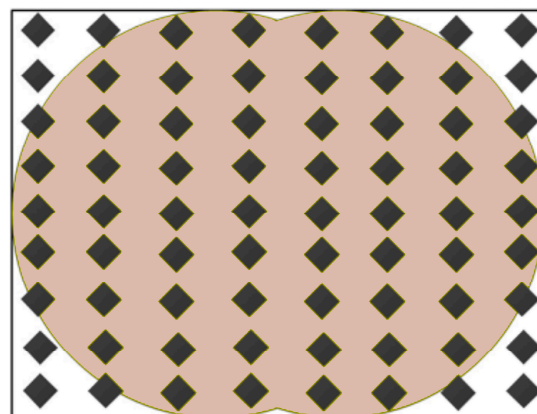

Figure 2. Sample points within the particle boundary surface.

Second, the position of each sample point in the fluid domain grid element is determined, and the solid volume fraction in a grid element is calculated as the proportion of sample points within the particle boundary surface to all points in the grid element, as follows:

$$\varepsilon_p = \sum_{Particles} \frac{n_c}{N}V_p \tag{5}$$

where ε_p represents the solid volume fraction, n_c represents the number of sample points in the particle grid element, N represents the number of sample points in the particle boundary surface, and V represents the whole particle volume, m^3.

In the CFD-DEM, the drag model describes the particle–fluid interaction. Therefore, the accuracy of the drag model ensures the accuracy of the CFD-DEM coupling simulation. Herein, the developed fluid–solid simulation based on the EDEM–Fluent coupling module mainly uses an improved freestream resistance model to calculate the interaction force on each sub-spherical particle. The freestream resistance of particles is calculated as follows:

$$\vec{F_D} = \frac{1}{8}\pi\rho_g d_p^2 C_D \left|\vec{v_r}\right|\vec{v_r} \tag{6}$$

where $\vec{v_r}$ represents the relative moving speed of particles, m/s; d_p represents the diameter of constituent sub-particles, m; ρ_g indicates the fluid density, kg/m^3; C_D represents the drag coefficient. The drag coefficient C_D depends on the particle Reynolds number Re_p, and it is calculated as follows:

$$C_D = \begin{cases} \frac{24}{Re_p}, Re_p \leq 0.5 \\ \frac{24\left(1+0.15Re_p^{0.687}\right)}{Re_p}, 0.5 < Re_p \leq 1000 \\ 0.44, Re_p > 1000 \end{cases} \tag{7}$$

A suitable coupling model can achieve the momentum exchange between continuous fluid and discrete particles. The momentum interaction term $\vec{R_{s,f}}$ can be obtained from the resistance between the two phases of fluid and solid to realize fluid–solid coupling, and it is calculated as follows:

$$\vec{R_{s,f}} = \frac{\sum_{i=1}^{n}\vec{F_{i,D}}}{\Delta V_{cell}} \tag{8}$$

where n represents the number of particles in the grid, ΔV_{cell} represents the grid volume, m^3; $\vec{F_{i,D}}$ represents the drag force on each particle in the grid, N.

2.3. Non-Analytical CFD-DEM Method Combined with BPM

During DEM-CFD coupling simulation, the particles are decomposed into many sampling points when calculating the solid volume fraction of particles (Figure 2). The solid volume fraction of particles in each grid is then determined based on the position of the sampling points on the grid. The momentum interaction term is also calculated based on the particle center position on the grid. Therefore, the solid volume fraction can be accurately calculated to multiple grids covered by particles if the particle volume is larger than the fluid domain grid, while the momentum interaction term can only be calculated to a single grid where the particle center is located (Figure 3a). Although the surrounding fluid domain grid occupies the solid volume fraction, the corresponding momentum interaction terms cannot be counted, resulting in deviations in the size and position of the fluid force acting on the particles.

This study developed a fluid–solid coupling calculation method based on a bonded-particle model (BPM) to solve the above problems. The method uses an aggregate of multiple sub-particles bonded by cohesive bonds instead of a whole particle. The volume of the sub-particles is smaller than the volume of the fluid domain grid (Figure 3b). Therefore, the theoretically established bonded-particle model can meet the requirements of non-analytical CFD-DEM. The fluid force on each sub-particle can be transmitted through the cohesive bond, making the sub-particles maintain a unified motion state in a macroscopic view.
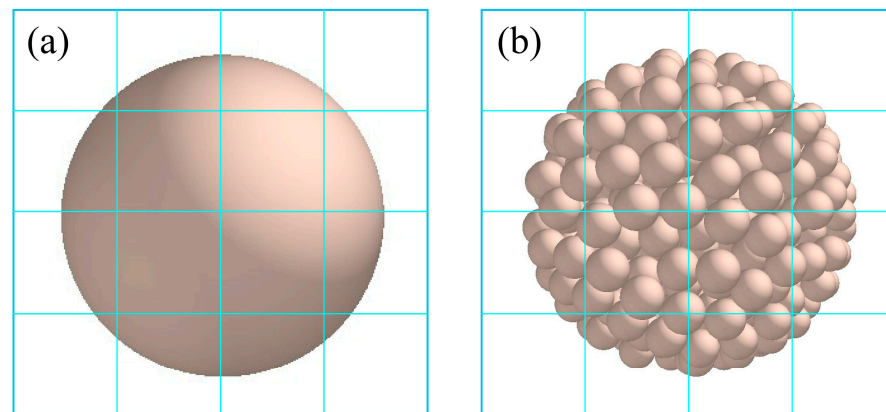
Figure 3. Comparison between particle volume and fluid domain grid volume. (**a**) The particle volume is larger than the mesh volume, (**b**) the particle volume is smaller than the mesh volume.

Unlike the analytical CFD-DEM method used to calculate the fluid force on particles, the established bonded-particle model has a limitation, i.e., the filling volume fraction of sub-particle aggregate to the whole particle is less than 1. The real density of the particles measured through experiments cannot be used after the sub-particles have been bonded. Therefore, the density of the sub-particles that make up the bonded-particles should be corrected to ensure the ratio of the total fluid drag force on the bonded-particles to the drag force on the particles before replacement is equal to the ratio of mass to ensure the accuracy of the movement of the bonded-particles. The density can be corrected as follows:

$$\rho_a = \frac{\rho_{Real} \cdot V_{Real}}{N \cdot V_F} \tag{9}$$

where ρ_{Real} represents the real density before particle replacement; V_{Real} represents the volume before particle replacement; ρ_a indicates the corrected density of the constituent sub-spherical particles; V_F indicates the volume of the constituent sub-spherical particles; N represents the number of constituent sub-spherical particles. This paper used the corrected particle density for the simulation of bonded-particles.

The number and size of the sub-particles directly affect the accuracy of the bonded-particle method. This paper used surface roughness to represent the accuracy of the seed particle model. The particle surface roughness is the ratio of the constituent sub-particle diameter to the whole particle diameter. Therefore, the surface accuracy of the particle model can be improved by increasing the number of constituent sub-particles when establishing the bonded-particle model of pelleted vegetable seeds. However, the calculation cost will be increased [20–22]. Herein, the simulation pre-test showed that pelleted vegetable seed particles had 36 sub-spheres, 50 sub-spheres, 70 sub-spheres, 109 sub-spheres, and 164 sub-spheres, expressed as BS (0.125), BS (0.1125), BS (0.1), BS (0.0875), and BS (0.075), respectively, based on the bonded-particle surface roughness (Table 2).

Table 2. The bonded-particle surface roughness.

Type	Seed Bonded-Particle Model				
Number of sub-spheres	36	50	70	109	164
Diameter of sub-spheres	0.5	0.45	0.4	0.35	0.3
Surface roughness	0.125	0.1125	0.1	0.0875	0.075

3. Materials and Methods

3.1. Test Materials

This study obtained the pelleted vegetable seeds (sphericity, 97.6%, and particle size, 4.0 ± 0.1 mm) from Weifang Agricultural Technology Co., Ltd. (Weifang, China). The

whole kernel oven method was used to determine the moisture content of the samples (10.9%). The experimental components used to analyze seed accumulation, flow behavior, and mixing characteristics were 3D-printed from photosensitive resin and transparent plexiglass. The 3D printing technology is widely used in laboratory test systems because it can directly, automatically, quickly, and accurately design models into target parts.

3.2. Seed Accumulation, Mixing, and Flow Behavior Experiments

This study compared the experimental and simulation results of the angle of repose, slope screening, and rotating container to verify the feasibility of using the bonded-particle method to model seed particles and evaluate the accuracy of population particle accumulation, mixing, and flow behavior. The established seed bonded-particle model was simulated using EDEM. The simulation parameters were determined using pre-experiments (Table 3). In addition to setting contact parameters, bonded-particle parameters should also be set (Table 4). It should be noted that the critical normal and shear strengths between sub-particles need to be set sufficiently high to prevent the bonded-particle model from breaking due to excessive local airflow forces in the flow field domain. In this paper, the critical normal and shear strengths between sub-particles in the bonded-particle model were both set to 1.0×10^{20} Pa.

Table 3. Simulation parameters.

Parameters	Symbols	Particle	Photosensitive Resin	Transparent Plexiglass
Density, kg/m^3	ρ	1340	1800	1600
Poisson's ratio	υ	0.4	0.35	0.35
Shear modulus, Pa	G	1.50×10^8	1.30×10^9	1.30×10^9
Coefficient of restitution	e	0.526	0.627	0.643
Coefficient of static friction	μ	0.297	0.41	0.45
Coefficient of rolling friction	μ_r	0.03	0.026	0.032

Table 4. Bonded-particle parameter.

Parameters	Numerical Value
Normal stiffness per unit area, N/m^3	1.0×10^8
Shear stiffness per unit area, N/m^3	5.0×10^7
Critical normal strength, Pa	1.0×10^{20}
Critical shear strength, Pa	1.0×10^{20}

3.2.1. Angle of Repose

The angle of repose experiment was used to evaluate the accumulation behavior of the developed seed bonded-particle model. The schematic representation of the angle of repose experimental apparatus is shown in Figure 4. The angle of repose experiment was conducted as follows: First, 0.1 kg of pelleted vegetable seed particles was poured into the area above the angle of the repose tester, while the surface of the population particles was kept flat. Second, the fixed board was removed at 1 m/s, making the population particles flow from the upper box. Finally, the accumulation images of population particles were obtained from the front when the whole population of particles stopped moving and appeared to be stable. The non-linear least square method was used to fit the angle of repose formed by the seed population particles based on the Levenberg–Marquardt algorithm (LMA). The arctangent function value of the slope of the fitting line represented the experimental value of the angle of repose (Figure 5). Each experiment was repeated thrice, and the value obtained was averaged. The same preset conditions in the experiment were used in EDEM 2020 software. BS (0.125), BS (0.1125), BS (0.1), BS (0.0875), and BS (0.075) were selected for simulation. A computer equipped with Intel Core i7-11700F 2.5GHz CPU (Hasee Computer Ltd., Shenzhen, China) was used for simulation experiments.
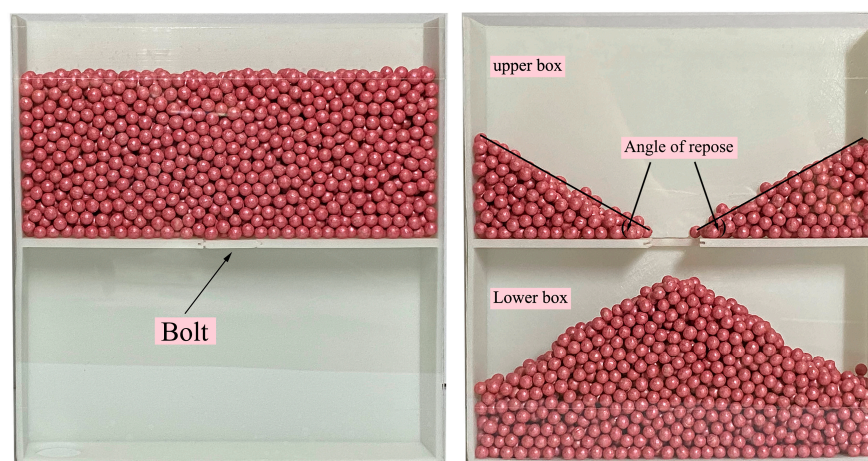
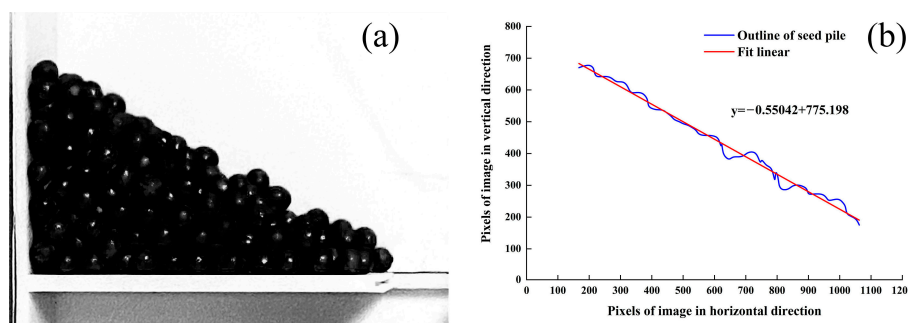**Figure 4.** Schematic representation of the angle of repose experimental apparatus.

Figure 5. The image processing method of the angle of repose. (**a**) Image binarization, (**b**) boundary fitting.

3.2.2. Slope Screening

Although the angle of repose experiment reflects the population accumulation effect of seed particles, it is not comprehensive enough. As a result, this study used the slope screening experiment to reflect the contact behavior between a single seed particle and the wall surface. Here, the seed particles on the sieve plate were screened to further analyze the feasibility and accuracy of the developed seed bonded-particle model. In the slope screening experiment, this study used a photosensitive resin (length: 300 mm, width: 150 mm, and thickness: 1 mm) as the sieve plate. The sieve hole diameter was selected as 4.2 mm [23]. The experimental inclination angle of the sieve plate was determined by determining the relationship between the inclination angle of the sieve plate and the total sieving percentage passing (Figure 6). The total sieving percentage passing was stable when the inclination angle of the sieve plate was greater than 10°. This study then selected the inclination angle of the sieve plate to be 10° for the slope screening experiment.

A receiving box with five sub-bins was placed under the sieve plate. The five sub-bins represented area 1, area 2, area 3, area 4, and area 5 from right to left (Figure 7). The slope screening experiment was conducted as follows: 50 g of seed particles was put into the loading area. The fixed insert plate was then removed at 1 m/s when the seed population was stable to allow the seeds to flow along the sieve plate due to gravity. The part of the seeds smaller than the hole diameter entered the receiving box through the sieve hole. The seed mass falling into each sub-interval was measured using an electronic balance (accuracy, 0.01 g) when the whole seed population stopped moving and appeared stable. The sieving percentage passing was also calculated. The sieving percentage passing is the percentage of the mass of the particles in the specified interval to the total mass of the given particles [24,25]. The same test setup and measurement procedures were used in the EDEM

simulations. BS (0.125), BS (0.1125), BS (0.1), BS (0.0875), and BS (0.075) were selected for simulation. Each experiment was repeated thrice, and the value obtained was averaged.
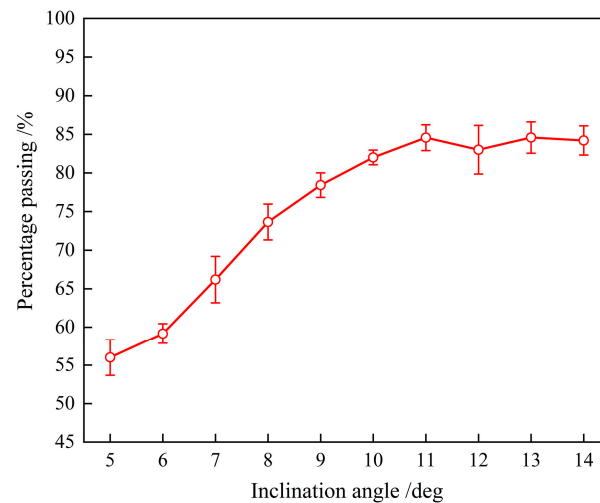

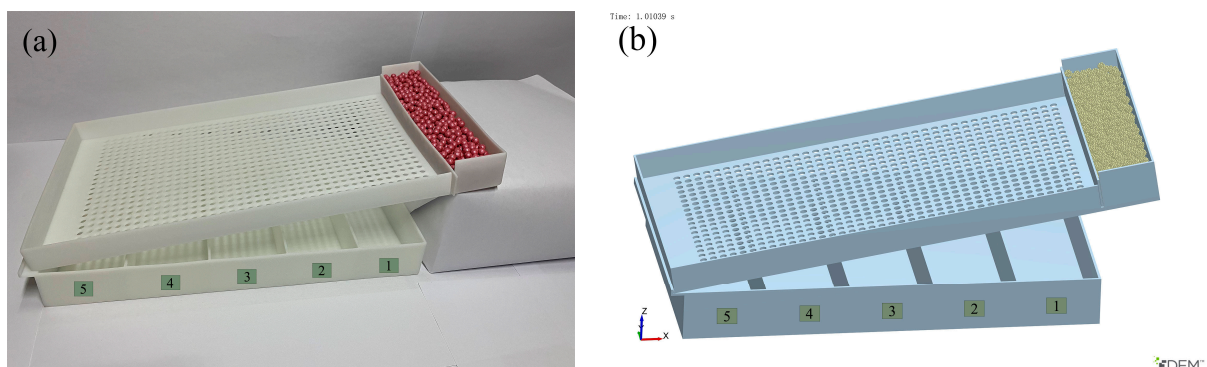**Figure 6.** Relationship between the total sieving percentage passing and the inclination angle.

Figure 7. (**a**) Experimental images and (**b**) simulation images in EDEM when the slope screening began.

3.2.3. Rotating Container

The rotating container is widely used in agricultural engineering fields, including material mixing, drying, and seed coating [26]. This study used a rotating container experiment to evaluate the mixing characteristics of the developed seed bonded-particle model. The experiment was conducted as follows: First, seed particles dyed with two colorants (50 g each) were placed on both sides of the rotating container pre-installed with a diaphragm to ensure that the filling rate of the seed population was more than 30% vol to visualize the flow pattern and mixing characteristics of the seed population particles (Figure 8). The diaphragm was then removed, and the rotating container was rotated at different speeds. A MS03130 high-speed camera (Ming Shiwei Ltd., Shenzhen, China) was used to record the mixing process of the seed population particles during the rotation. The non-linear least square method was used to fit the dynamic contour curve formed by the seed population particles based on the Levenberg–Marquardt algorithm (LMA) (Figure 9). The same test setup and measurement procedures were used in the EDEM simulations. BS (0.125), BS (0.1125), BS (0.1), BS (0.0875), and BS (0.075) were used for simulation. Notably, the seed population particles formed different flow states (collapsed state, rolling state, and cascade state) in the rotating container based on different rotation speeds. The seed population particles in the rolling state have more important practical application significance in agricultural engineering applications [27]. This study conducted the speed pre-test of the rotating container to ensure that the seed population particles were in the rolling state. Finally, 20 rpm, 40 rpm, and 60 rpm were selected as the rotation

speeds of the rotating container experiment. Each experiment was repeated three times, and the average value was taken as the result of the rotating container experiment.
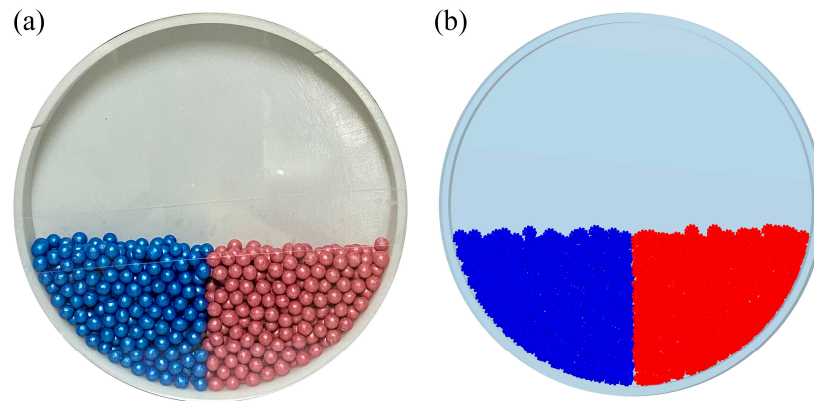

Figure 8. (**a**) Experimental images and (**b**) simulation images in EDEM when the rotating container began to rotate.
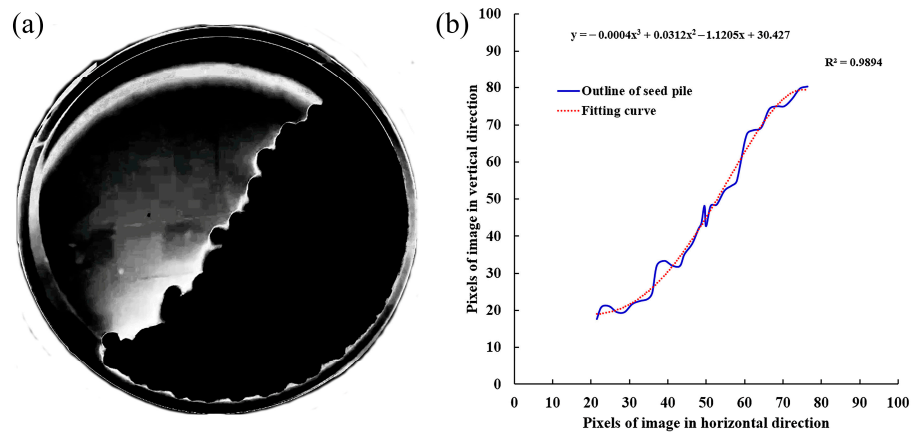

Figure 9. The image processing method of the rotating container. (**a**) Image binarization, (**b**) boundary fitting.

3.2.4. Particle Sedimentation Experiment

The bonded-particle model and non-analytical CFD-DEM methods were combined to simulate the settling motion of a single seed particle in the fluid under gravity. The calculation and the coupling simulation results were compared to verify the feasibility and accuracy of the established seed bonded-particle model in the DEM-CFD coupling calculation. EDEM–Fluent was used for the coupling simulation experiment of particle sedimentation. The coupling system program was mainly divided into the particle calculation part (DEM), fluid calculation (CFD), and data interaction. The EDEM program was used to calculate the motion information of seed particles, and the Fluent program was used to solve the fluid motion equation. The particle space position, movement speed, and other information calculated by the DEM solver were transmitted to the CFD solver during the calculation time coupling. The CFD solver calculated the drag force and buoyancy based on the porosity in the fluid element and the relative velocity between particles and fluid, then transmitted the information to the DEM solver for calculation, thus realizing the interactive transmission of CFD-DEM momentum, thereby completing the fluid–structure coupling calculation [28]. The detailed calculation process of fluid–structure coupling is shown in Figure 10.
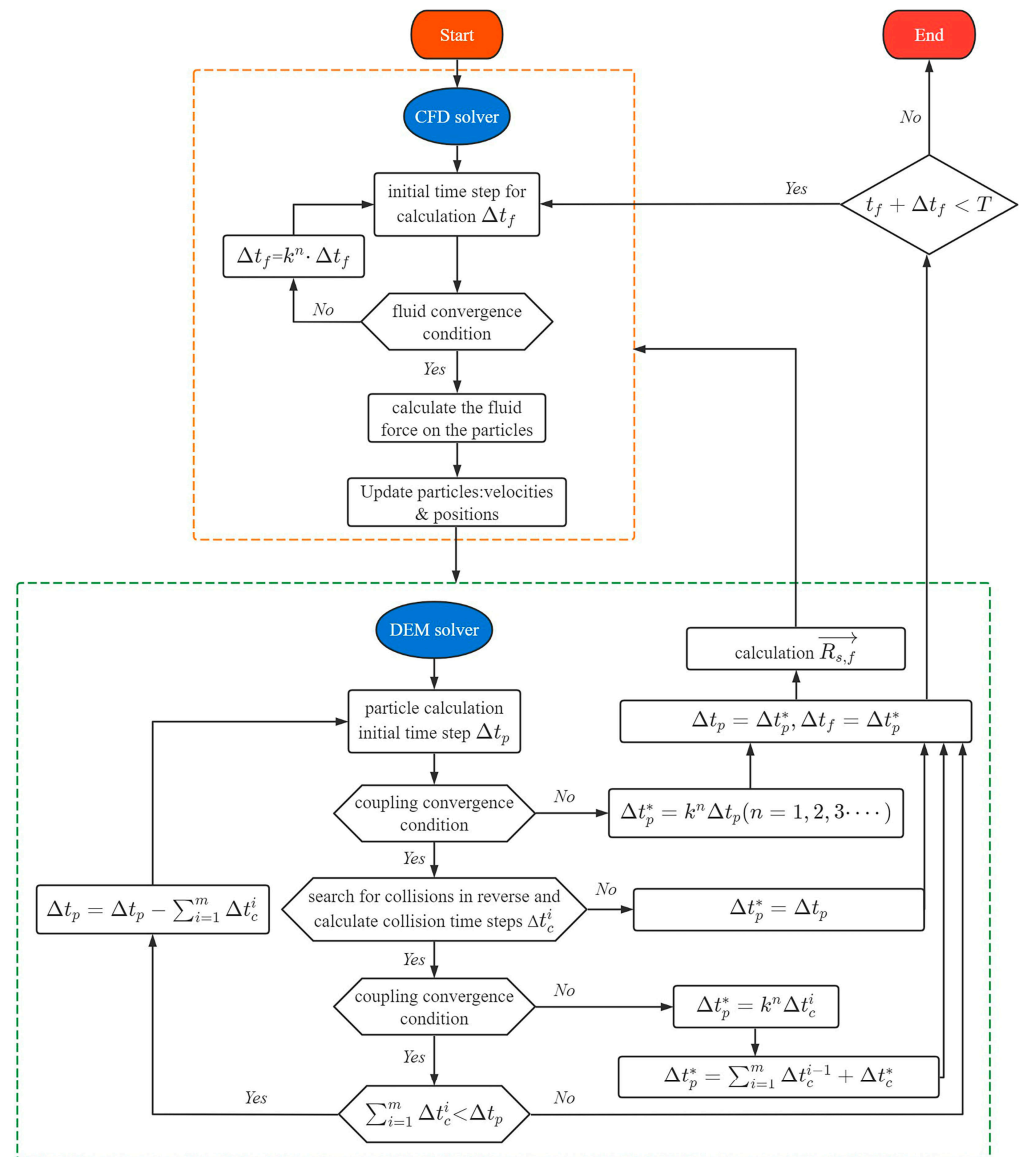
Figure 10. Flow chart of CFD-DEM coupling calculation.

The simulation fluid domain was divided into $10 \times 10 \times 40$ grids (side length of each grid; 3 mm and size of the whole fluid domain; 30 mm $\times$ 30 mm $\times$ 120 mm) (Figure 11). The seed bonded-particles were placed in a fluid with a viscosity coefficient of 0.01, and the particles fell freely due to gravity. The calculation time of CFD and DEM were set at 1×10^{-5} s and 1×10^{-6} s, respectively.

Stokes law states that the settling velocity of particles in fluid due to gravity is constant. Herein, the theoretical calculation results of the particle settling velocity in the fluid were based on Stokes particle-free precipitation formula, as follows:

$$V_s = \frac{2}{9} \frac{r^2 g \left(\rho_p - \rho_f \right)}{\eta} \tag{10}$$

where V_s represents the particle settling velocity, m/s; ρ_p represents the particle density, kg/m; ρ_f represents fluid density, kg/m; g represents gravity acceleration, m/s^2; η represents the viscosity coefficient of fluid, Pa·s; and r represents the particle radius, m.
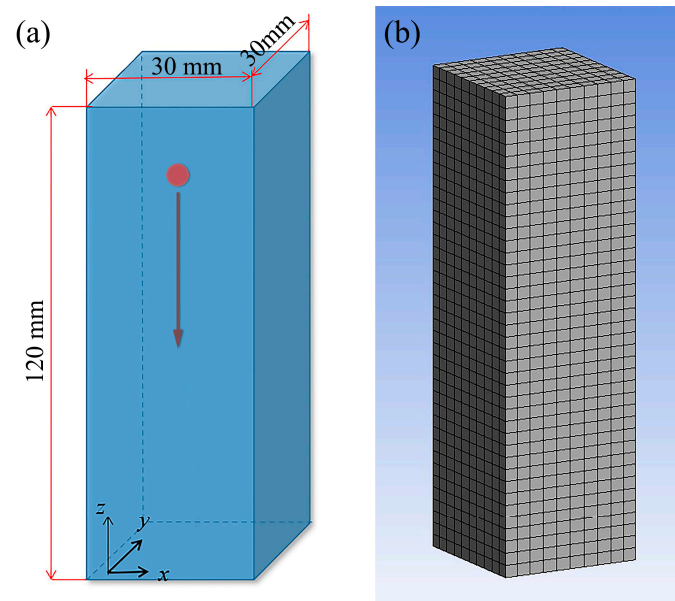
Figure 11. Schematic representation of particle settlement model. (**a**) Numerical model, (**b**) grid division of simulation fluid domain.

4. Results and Discussion

4.1. Angle of Repose Experimental Results and Discussion

Figure 12 shows comparisons of repose angles in the experimental and simulated snapshots. The repose angle formed by BS (0.125), BS (0.1125), BS (0.1), BS (0.0875), and BS (0.075) was fitted via the processing method in Figure 5 to obtain Figure 13. Figure 13 shows repose angle variations of the seed bonded-particle model with surface roughness (the red dotted line denotes the experimental average value of the repose angle, while the orange area denotes the error range of the experimental results). Based on the analysis of Figure 13, it can be concluded that, with decreasing surface roughness (that is, the increase in the number of constituent sub-spheres), the repose angle of the seed bonded-particle model gradually decreased, and the corresponding repose angle gradually approached the experimental results. This is because, when the sub-sphere number was relatively small, the shape of the seed bonded-particle model differed from the real seed. At this time, the occurrence of interlocking behaviors between seed particles was easy, and the repose angle from the simulation model was higher than the experimental repose angle. With the increasing number of sub-spheres in the seed bonded-particle model, surface roughness decreased while seed particle surface smoothness was enhanced. At this time, the particles' flow characteristics were improved, and the repose angle of the simulation model gradually approached the experimental repose angle. Specifically, when the surface roughness of the seed bonded-particle model was not greater than 0.1, that is, the number of constituent sub-spheres was not less than 70, the corresponding repose angle of the simulation model was within the standard deviation range of the experimental repose angle ($28.8° \pm 1.58°$). Based on the above analysis, the surface roughness of the seed bonded-particle model had a significant effect on the repose angle formed by the seed population particles. When the surface roughness of the seed bonded-particle model was not greater than 0.1, the simulation of the bonded-particle model established in this paper can reproduce the accumulation behavior of the seed population under the actual experimental repose angle.
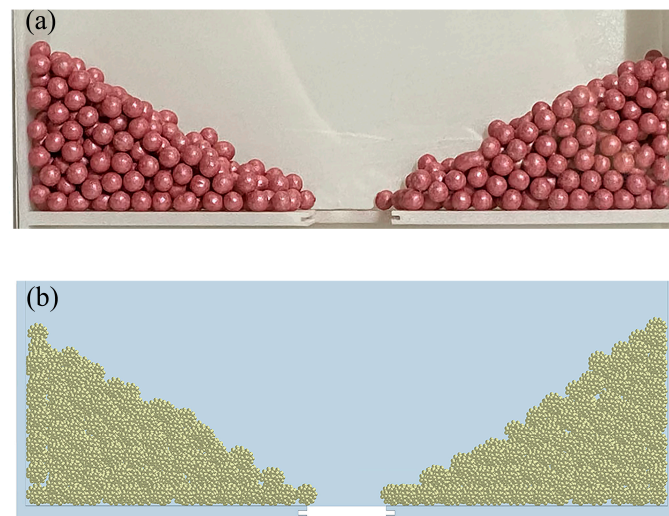
Figure 12. (**a**) Experimental snapshot and (**b**) simulation snapshots in EDEM during the formation of the repose angle.
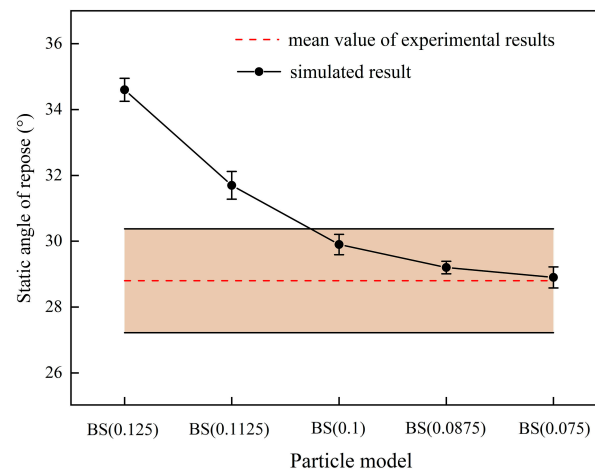

Figure 13. Variations of repose angle of the seed bonded-particle model with surface roughness.

4.2. Slope Screening Experimental Results and Discussion

Figure 14 shows the comparisons of the slope screening experimental snapshot and the simulated snapshot. Experimental and simulation slope screening results of BS (0.125), BS (0.1125), BS (0.1), BS (0.0875), and BS (0.075) were counted to obtain Figure 15. From Figure 15, change trends of the simulated sieving percentage passing of the bonded-particle model under different surface roughness were consistent with change trends of the experimental sieving percentage passing. Among them, simulation results of BS (0.1), BS (0.0875), and BS (0.075) were very close to experimental results. The BS (0.125) simulation results exhibited a large error relative to experimental results, while relative errors between simulation and experimental results in sub-interval 1 and area 2 were 28.71% and 19.74%, respectively. In addition, with increasing counts of sub-spheres composed of seed bonded-particle model, the overall sieving percentage passing of sub-interval 1 exhibited a downward trend. This was attributed to the fact that, as the number of bonded-particle model sub-spheres increased, the associated surface roughness decreased, and seed particle fluidity on the sieve plate was enhanced by various degrees. Therefore, the number of seed particles passing through sub-interval 1 decreased, while the number of seed particles passing through the other sieve holes gradually increased. In conclusion, the surface roughness of the seed bonded-particle model exerted significant effects on the screening process of seed population particles. When the seed bonded-particle model's

surface roughness was not greater than 0.1, the slope screening simulation of the seed bonded-particle model was very close to the experimental results. When the surface roughness of the bonded-particle model was set to 0.075, the discrepancy between the number of seed particles passing through sub-interval 1 and the measurement results was a mere 1.52%, with passing rates of 51.41% and 52.19%, respectively. In general, slope screening simulation using the established bonded-particle model established in this paper accurately reflected the screening process of actual seed population particles.
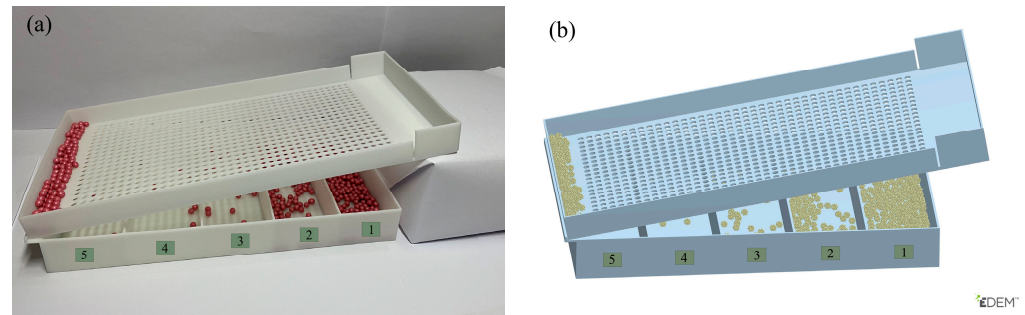
Figure 14. (**a**) Experimental photo and (**b**) simulation snapshots in EDEM upon completion of slope screening.
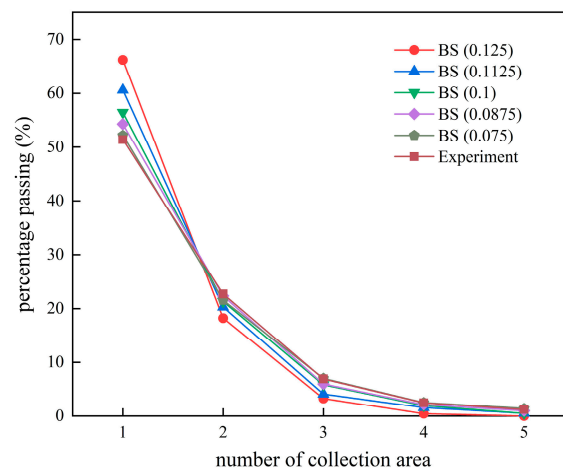

Figure 15. Variations of sieving percentage passing of seed bonded-particle model with different surface roughness in each sub-interval.

4.3. Rotating Container Experimental Results and Discussion

For visual analysis of the mixing behaviors of seed population particles in the rotating container, pelletized vegetable seed particles dyed with red and blue colorants were placed on both sides in equal amounts and the rotating speeds of the container were set to 40 rpm. Comparisons between the experimental snapshot and simulated snapshot after 1, 1.5, and 2 revolutions of the rotating container are shown in Figure 16. In the simulation and experimental mixing process of the rotating container, relative positional relationships between red and blue seed population particles were roughly the same. Simulated flow patterns of seed population particles were in good agreement with experimental flow patterns, which qualitatively verified that the bonded-particle method-established seed particle model can reasonably reproduce flow behaviors and mixing characteristics of seed population particles in the rotating container.
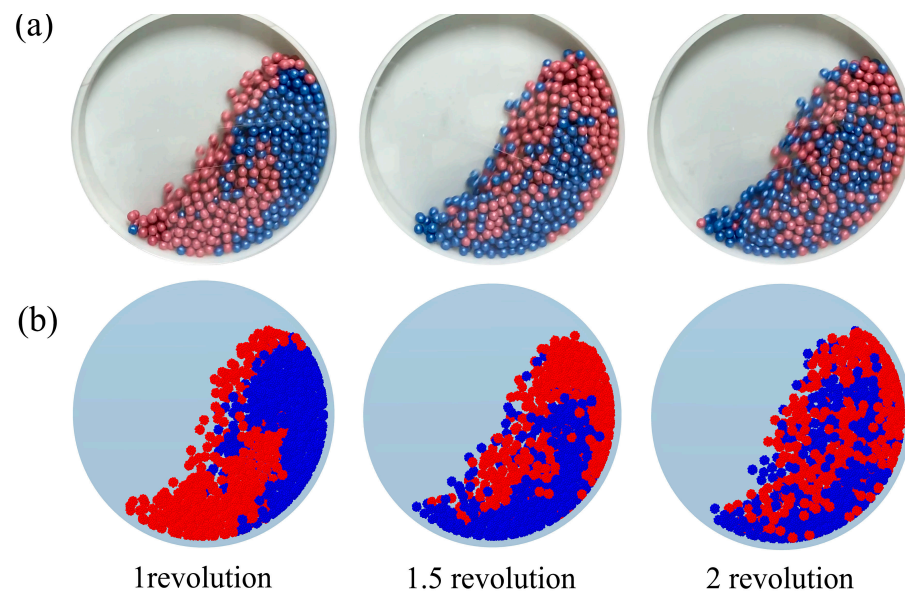
Figure 16. Comparison of the simulated flow pattern with experiments at the rotation speed of 40 rpm for pelletized vegetable seeds. (**a**) Experiment, (**b**) simulation.

To evaluate the accuracy of the seed bonded-particle model, simulation and experimental images of various mixing stages were divided using 5×5 mm square cells, after which the mixing characteristics of seed population particles in the rotating drum under different rotation cycles were quantitatively analyzed via the Lacey mixing index [29].

$$M = \left(S_0^2 - S^2 \right) / \left(S_0^2 - S_r^2 \right) \tag{11}$$

where S_0^2 and S_r^2 represent the variance when red and blue seed population particles were completely separated and completely mixed, respectively, $S_0^2 = p(1 - p)$; $S_r^2 = p(1 - p)/N$. p denotes the proportions of seed particles of the selected color in the seed population; N represents the average number of seed particles in a single sample square; S^2 is the variance of the mixed state of the seed population at the current moment. Given the variations in the number of seeds in each sample square, the weighted method was used for calculation, that is, the weights of the large number of seeds in the sample grid were relatively high, the weights of the small number of seeds were relatively low, and the weight of the sample grid without seeds was 0.

Figure 17 shows the variations in the Lacey mixing indices of seed population particles in the rotating container under different rotation cycles. The simulation and experimental Lacey mixing indices of seed population particles first exhibited an increasing trend, which gradually approached 1 as the number of rotations of the container increased. Among them, the Lacey mixing index gradually converged after the container rotated for four revolutions. At this time, seed population particles, as a whole, reached the mixing limit. This change phenomenon was comparable to the particle mixing change trend obtained in previous studies [30–32]. At a rotation speed of 40 r/min and with bonded-particle modeling schemes of BS (0.125), BS (0.1), and BS (0.075), the average values of the stabilized Lacey mixing index were 91.39%, 90.55%, and 89.92%, respectively. The differences from the measurement results (85.57%) were 6.80%, 5.82%, and 5.08%, respectively. In addition, the simulation results of BS (0.075) were closest to the experimental Lacey mixing index. This was attributed to the fact that when fewer sub-spheres were used for the construction of the bonded-particle model, the particle model's surface roughness was relatively large, which increased the rotation resistance of the seed bonded-particle model. When more sub-spheres were used for the construction of the bonded-particle model, particle surface smoothness was enhanced, and the rotation resistance of the particle model became close to

actual particles. After the seed population particles reached the mixing limit, the fluctuation degree of the Lacey mixing index was proportional to the rotation speed of the container.
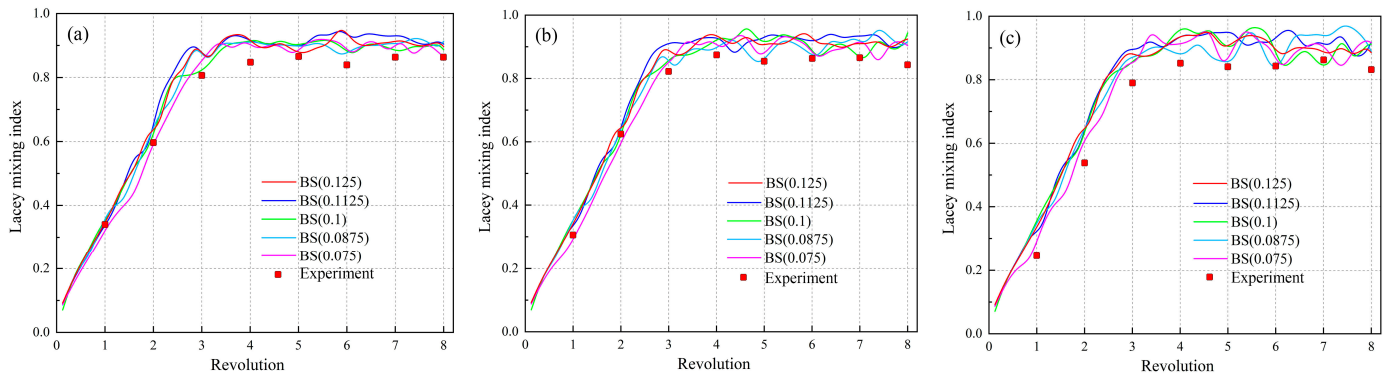

Figure 17. Quantification of simulated and experimental Lacey mixing indices. (**a**) 20 r/min, (**b**) 40 r/min, (**c**) 60 r/min.

To intuitively compare the dynamic profiles of seed population particles under different surface roughness, after stabilization of the mixing process of seed population particles in the rotating container, the single simulation and experimentally obtained images were processed. Scanning of surface contours of seed population particles in the rotating container was performed by detecting pre-defined pixels in the RGB color interval of the image. Pixel position information on the surface of the scanned population particle contour was fitted using the least square method. At different rotational speeds, the dynamic contour fitting curve of the rotating container is shown in Figure 18. At 20 rpm, the simulated dynamic profile curves of BS (0.125) and BS (0.1125) exhibited a large deviation from experimental results, while the other simulation dynamic contour curves at different speeds were basically comparable to experimental dynamic contour curves. This was because the accuracy of the repose angle under BS (0.125) and BS (0.1125) models was low. Therefore, when the overall behaviors of seed population particles were more static, there were large deviations between simulated and experimental dynamic contour curves. In addition, dynamic contour curves of seed population particles became steeper with increasing rotating speeds of the container. In summary, the seed particle model, which was built via the bonded-particle method, can accurately reproduce flow behaviors and mixing characteristics of seed particles in the rotating container, and its simulation accuracy improves with an increasing number of constituent sub-spheres.
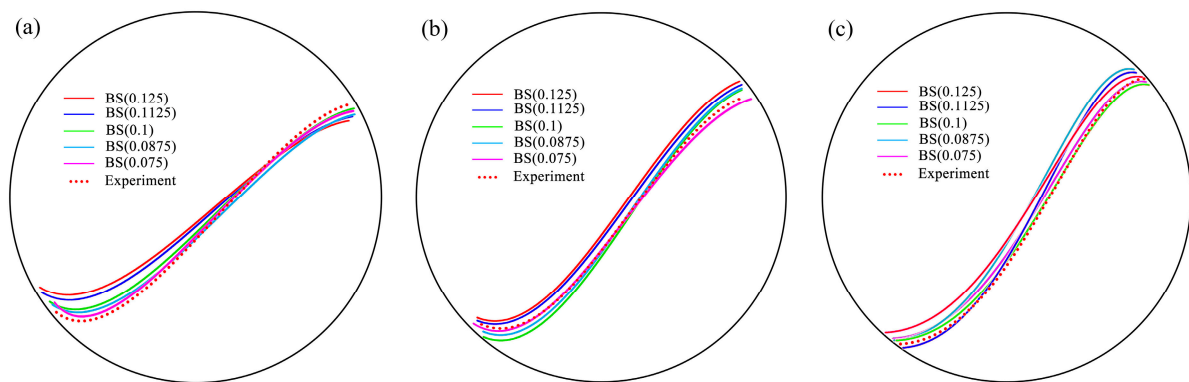

Figure 18. Dynamic contour fitting curve of the rotating container at different rotational speeds. (**a**) 20 r/min, (**b**) 40 r/min, (**c**) 60 r/min.

4.4. Particle Sedimentation Experimental Results and Discussion

Figure 19 shows the variation curve of the settling velocity of the seed bonded-particle model with time in the fluid. The results of particle settling velocity with different surface roughness during the particle settling process are shown in Table 5. Within a short time, the settling velocity rapidly increased and tended to remain at a constant value. This was because, when seed particles initially settled, then, under the influence of their own gravity, settling velocities of the particles rapidly increased, which increased drag forces on particles, thereby bringing the drag force closer and closer to the floating gravity of particles (gravity minus buoyancy). Finally, the drag force on the particles became consistent with floating gravity, which balanced the overall force. At this time, particle acceleration was 0, while its settling velocity did not change. With the decreasing surface roughness of the seed bonded-particle model, the final settling velocity was closer to the theoretical value (-0.296 m/s). When the surface roughness of the bonded-particle model was set to 0.075, the discrepancy between the final settling velocity of the particles and the theoretically calculated value was just 1.01%. This was because the smaller the surface roughness of bonded-particles, the smaller the sizes of constituent sub-spheres, the larger the size ratio of the fluid domain grid to particles, and therefore, the higher the coupling accuracy. Second, the larger the surface roughness of bonded-particles, the smaller the number of sub-spheres. At this time, the surfaces of bonded-particles were relatively unsmooth, which increased the rotation resistance of the particle model, ultimately affecting the sedimentation behaviors of seed particles. In general, the seed particle model established by the bonded-particle method can accurately reproduce the sedimentation movements of particles, and the accuracy of coupling simulation increases with an increasing number of constituent sub-spheres.
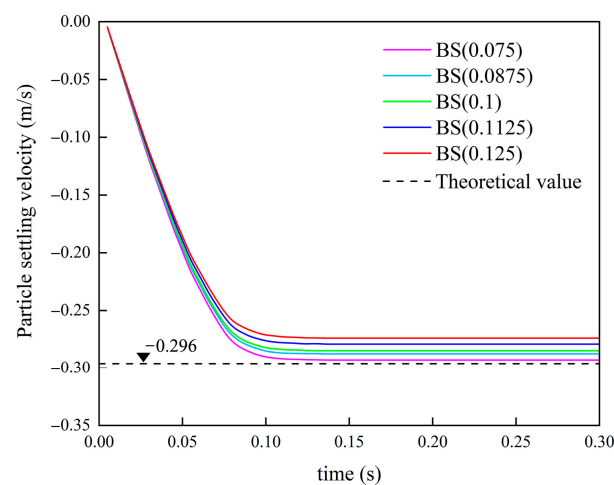

Figure 19. Variation curves of settling velocity of the seed bonded-particle model with time in the fluid.

Table 5. Particle settling velocity results with different surface roughness.

Particle Settling Time (s)	Particle Settling Velocity (m/s)				
	BS (0.075)	BS (0.0875)	BS (0.1)	BS (0.1125)	BS (0.125)
0.05	−0.198	−0.195	−0.193	−0.189	−0.185
0.10	−0.290	−0.285	−0.282	−0.276	−0.271
0.15	−0.293	−0.287	−0.285	−0.279	−0.274
0.20	−0.293	−0.288	−0.285	−0.279	−0.274

During the precise sowing procedure of the air-suction seed-metering system, several inter-population interactions took place within the internal working region. The procedure of simulating the precision seeding process of an air-suction seed-metering system using DEM-CFD was a time-consuming task. The quantity of sub-spheres in the bonded-particle model played a vital role in defining the duration of the coupling calculation. While

constituent sub-spheres can improve the accuracy of coupling simulations for seed particle sedimentation, they also come with a substantial increase in the computational cost of coupling. Figure 20 displays the ratio of the computation time for coupling in the bonded-particle model to that of the spherical particle model (with a diameter of 0.3 mm). The computation time of the bonded-particle model exhibited a clear correlation with the quantity of constituent sub-spheres. The increase in the number of sub-spheres in the coupling calculation process led to a non-linear increase in contact judgment between particles, cohesive bond force, and momentum information transmission. This, in turn, increased the time required for the calculation of particle positions and other information, thus prolonging the overall simulation time. Overall, the utilization of the BS (0.1) bonded-particle model can improve the precision of the sedimentation motion of seed particles and guarantee a relatively efficient calculation process.
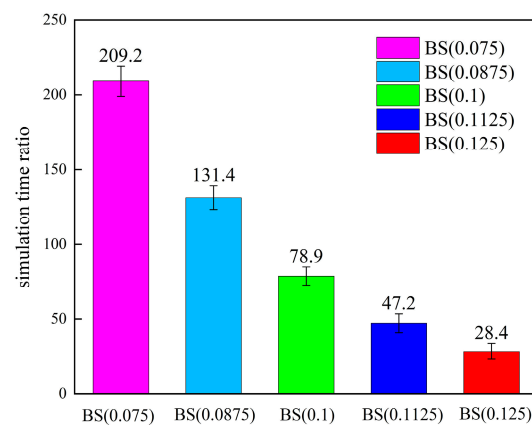
Figure 20. Coupling calculation time ratio of the bonded-particle model and single sub-spherical particle.

5. Application

An application case was used to show how to employ the pelleted vegetable seed bonded-particle model and the DEM-CFD coupling method to analyze the working process and performance of a machine [33]. The three-dimensional structure and division of working areas for the air-suction seed-metering device are depicted in Figure 21. During the precision sowing process, the seeds in the seed-filling region are stirred up by the spinning seed-metering plate. The seed-filling region utilizes negative pressure airflow to draw in one or more seeds through the suction holes on the seed-metering plate. These seeds then move to the transition area as a result of collisions and extrusions between different seed populations. Afterward, one or more seeds that are consistently located in the suction hole are transported to the seed-clearing region through the rotational motion of the seed-metering plate. The blade teeth of the seed-cleaning device efficiently eliminate several seeds that are securely held in the suction holes, guaranteeing that only one seed may be consistently absorbed by the suction holes after passing through the seed-clearing area. In the end, the seed that is adsorbed singly on the suction hole rotates around its circumference, moving over the area where seeds are carried before finally reaching the area where seeds are unloaded. At the same time, the negative pressure dissipates, causing the seeds to move in a controlled manner into the seed guide tube because of the combined effects of gravity and centrifugal force, resulting in accurate planting.

The pelleted vegetable seed bonded-particle model referred to as the BS (0.1) model, was used for conducting gas–solid coupling simulation tests in this study. The working parameters were set based on the fluid domain features of the working process in the seed-metering device. The CFD Domin structure division is shown in Figure 22. The mesh area properties of suction holes were designated as moving meshes, employing the sliding mesh technique, whereas the remaining areas were assigned as static meshes. The contact surfaces of the suction holes, located between the seed chamber and the air chamber, were established as an interface. This setup facilitated data exchange between the two chambers

during the rotation of the seed-metering plate, thereby positioning the seed plate. The airflow field model boundary bar inlet pressure was set to -3 kPa. The rotation speed of the seed-metering plate was 30 rpm (with a forward working speed of 10.8 km/h and plant spacing of 0.1 m), the number of vegetable seed particles was 800, and the total number of particles after replacement with the bonded-particle model was 5.6×10^4. The gas–solid coupling simulation process of the air-suction seed-metering device is shown in Figure 23.
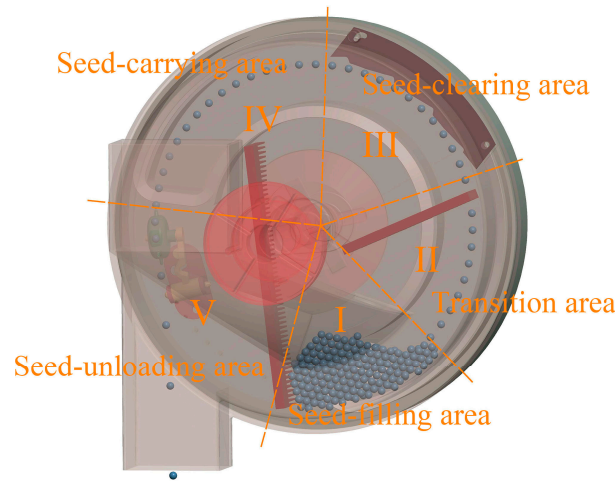
Figure 21. Division of working areas for the air-suction seed-metering device.
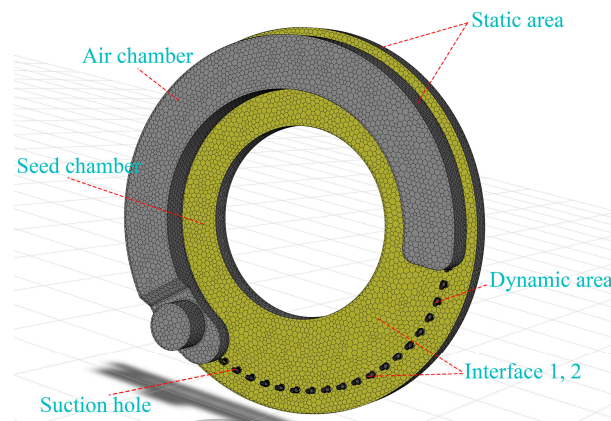
Figure 22. CFD Domin.
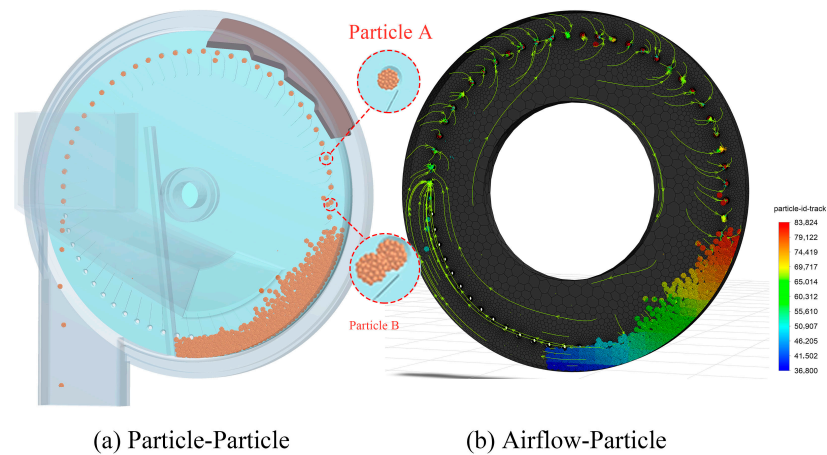
(a) Particle-Particle

(b) Airflow-Particle

Figure 23. Simulation process of gas–solid coupling.

Figure 23 depicts the process of adsorption and separation of bonded-particle seed populations within the air-suction seed-metering device system. Figure 23b illustrates the correlation between seed particles and the airflow patterns in the flow field. Because the DEM-CFD coupling simulation was bidirectional, particles were subjected to the drag force exerted by the airflow, causing them to be stably absorbed into the suction holes. At the same time, the airflow experienced resistance from particles that impeded its movement, and the drag force counteracted this resistance in the opposite direction. Figure 23 shows the selection of seed A, which is adsorbed as a single particle, and seed B, which is adsorbed as many particles, by the suction hole. Using the post-processor tool, we exported the data on the drag force and velocity change for both particle A and particle B. This process generated a radar map, which is shown in Figure 24. Examination of Figure 24 reveals a consistent increase in the overall drag force throughout the seed-filling and cleaning process (from 0 s to 0.76 s). Particle B, located in the seed-cleaning region at 0.64 s, impacted the teeth of the seed-cleaning blade. Afterward, the velocity and drag force experienced a rapid surge, eventually reaching a steady state after 0.76 s. The observed phenomenon can be attributed to the gradual displacement of particle B, which eventually became the dominant species in the adsorption process during cleaning. Figure 24 indicates consistency between the relationship of particle velocity and drag force on the particles, including their changing trends, and the seed movement mechanism in the air-suction seed-metering device. This verifies the feasibility and effectiveness of the bonded-particle modeling method for pelleted vegetable seeds.
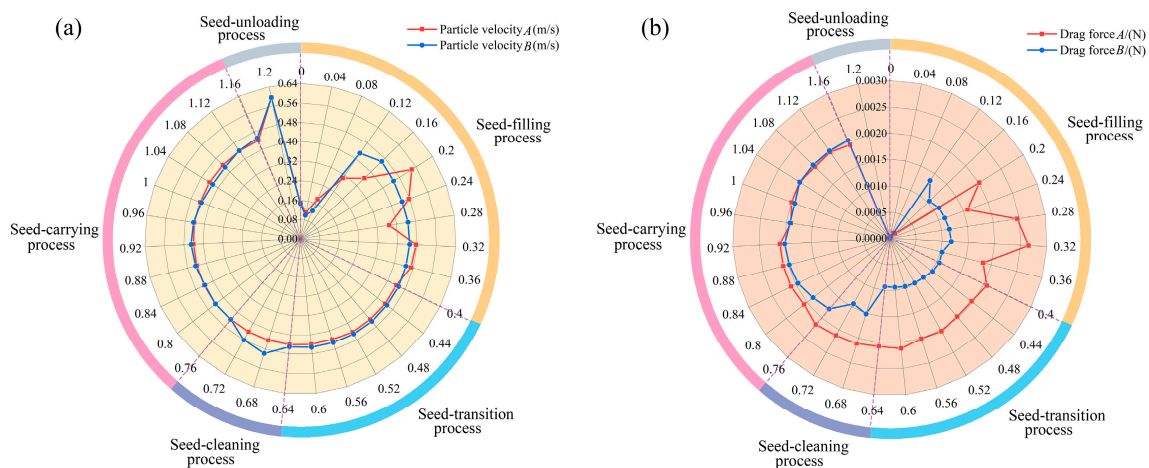

Figure 24. Results of gas–solid coupling: (**a**) drag force; (**b**) particle velocity.

The research above demonstrates that the complete precision seeding process of the air-suction seed-metering device can be replicated by utilizing the seed bonded-particle model and the DEM-CFD coupling method. The vegetable seed bonded-particle model, developed using BS (0.1), accurately predicts the performance of air-suction seed-metering devices during the initial design phase. It also offers valuable insights for designing and optimizing the major components of these devices.

6. Conclusions

To accurately simulate the precision seeding process of the population in the air-suction seed-metering device based on the discrete element method (DEM) and computational fluid dynamics (CFD), a method combining non-analytical CFD-DEM with BPM was proposed to establish the seed particle model. The accumulation process, flow behavior, mixing characteristics, and fluid–solid coupling motion of the seed bonded-particle model were analyzed through simulation, repose angle, slope screening, rotating container, and particle sedimentation experiments, thus verifying the feasibility and effectiveness of the proposed bonded-particle modeling method. In addition, the coupling accuracy and calcu-

lation efficiency of the seed particle model were assessed by evaluating the sedimentation movements of the seed particle model in the fluid. The main conclusions are as follows:

(1) The bonded-particle model of pelleted vegetable seeds was proposed and established. In detail, the number of constituent sub-spheres of the bonded-particle model was set to 36 spheres, 50 spheres, 70 spheres, 109 spheres, and 164 spheres, respectively. Moreover, surface roughness for each particle model was defined and calculated to represent the filling accuracy of the particle model, and was established to be 0.125, 0.1125, 0.1, 0.0875, and 0.075, respectively.

(2) The analysis of the angle of repose, slope screening, and rotating container, based on both simulation and experimental data, demonstrated that the surface roughness of the pelleted vegetable seed bonded-particle model had a substantial impact on the flow behavior and mixing features of the seed population. As the seed bonded-particle model's surface roughness lowered, the simulation findings aligned more closely with the experimental data. When the surface roughness of the seed bonded-particle model was equal to or below 0.1, the influence of the surface roughness of the seed model on the flow behavior and mixing features of the seed population was reduced. Specifically, when the surface roughness of the seed bonded-particle model was not greater than 0.1, or in other words when the number of constituent sub-spheres was not less than 70, the corresponding repose angle of the simulation model fell within the standard deviation range of the experimental repose angle ($28.8° \pm 1.58°$). When the surface roughness of the bonded-particle model was set to 0.075, the discrepancy between the number of seed particles passing through sub-interval 1 and the measurement results was a mere 1.52%, with passing rates of 51.41% and 52.19%, respectively. At a rotation speed of 40r/min and with bonded-particle modeling schemes of BS (0.125), BS (0.1), and BS (0.075), the average values of the stabilized Lacey mixing index were 91.39%, 90.55%, and 89.92%, respectively. The differences from the measurement results (85.57%) were 6.80%, 5.82%, and 5.08%, respectively.

(3) The seed particle model, constructed by the bonded-particle method, can precisely simulate the sedimentation motion of particles. Moreover, the precision of the coupling simulation was enhanced with the augmentation of the number of constituent sub-spheres. When the surface roughness of the bonded-particle model was adjusted to 0.075, the difference between the actual settling velocity of the particles (-0.293 m/s) and the theoretically estimated value (-0.296 m/s) was just 1.01%. After a thorough evaluation of the expenses associated with coupling calculations, the most suitable seed bonded-particle modeling scheme was identified to be BS (0.1), with a total of 70 constituent sub-spheres.

(4) The completed bonded-particle modeling scheme was used to demonstrate the applicability of the pelleted vegetable seed bonded-particle model and the DEM-CFD coupling approach in simulating and analyzing the precise sowing process of the air-suction seed-metering apparatus. Particle B, located in the seed-cleaning region at 0.64 s, impacted the teeth of the seed-cleaning blade. Afterward, the velocity and drag force experienced a rapid surge, eventually reaching a steady state after 0.76 s. The results demonstrated a correlation between the velocity of particles and the drag force acting on them, as well as the changing patterns of these variables. This correlation was also consistent with the process by which seeds were moved in the air-suction seed-metering device system. This study validates the practicality and efficiency of the bonded-particle modeling technique for pelleted vegetable seeds. In future research, the bonded-particle model and DEM-CFD coupling method will be used to further investigate the physical phenomena and mechanical properties of seeds as they move within the flow field of an air-suction seed-metering apparatus.

J.X. and W.W.; writing—review and editing, J.X., W.W., Z.Z. and T.T.; visualization, J.X. and C.H.; supervision, W.W.; project administration, W.W. and J.X.; funding acquisition, W.W. and J.X. All authors have read and agreed to the published version of the manuscript.

Institutional Review Board Statement: Not applicable.

Data Availability Statement: The data presented in this study are available upon request from the first author J.X.

Conflicts of Interest: The authors declare no conflicts of interest.

References

1. Cundall, P.A.; Strack, O.D.L. A discrete numerical model for granular assemblies. *Géotechnique* **1979**, *29*, 47–65. [CrossRef]
2. Lei, X.; Liao, Y.; Zhang, Q.; Wang, L.; Liao, Q. Numerical simulation of seed motion characteristics of distribution head for rapeseed and wheat. *Comput. Electron. Agric.* **2018**, *150*, 98–109. [CrossRef]
3. Yang, Q.; Li, Z.; Li, H.; He, J.; Wang, Q.; Lu, C. Numerical analysis of particle motion in pneumatic centralized fertilizer distribution device based on CFD-DEM. *Trans. Chin. Soc. Agric. Mach.* **2019**, *50*, 81–89. [CrossRef]
4. Choi, J.I.; Oberoi, R.C.; Edwards, J.R.; Rosati, J.A. An immersed boundary method for complex incompressible flows. *J. Comput. Phys.* **2007**, *224*, 757–784. [CrossRef]
5. Peskin, C.S. The immersed boundary method. *Acta Numer.* **2002**, *11*, 479–517. [CrossRef]
6. Mao, J.; Zhao, L.H.; Liu, X.N.; Di, Y.T. A resolved CFDEM algorithm based on the immersed boundary for the simulation of fluid-solid interaction. *Powder Technol.* **2020**, *374*, 290–303. [CrossRef]
7. Zhao, P.; Xu, J.; Ge, W.; Wang, J. A CFD-DEM-IBM method for Cartesian grid simulation of gas-solid flow in complex geometries. *Chem. Eng. J.* **2020**, *389*, 124343. [CrossRef]
8. Kou, J.; Joshi, S.; Hurtado-de-Mendoza, A.; Puri, K.; Hirsch, C.; Ferrer, E. Immersed boundary method for high-order flux reconstruction based on volume penalization. *J. Comput. Phys.* **2021**, *448*, 110721. [CrossRef]
9. Yang, Y.; Balachandar, S. A scalable parallel algorithm for direct-forcing immersed boundary method for multiphase flow simulation on spectral elements. *J. Supercomput.* **2021**, *77*, 2897–2927. [CrossRef]
10. Xiong, S.; Zang, M. Efficient simulation about the motion of large particles in fluid based on unresolved computational fluid dynamics and discrete element method. *Sci. Tech. Engrg.* **2021**, *21*, 6140–6146. [CrossRef]
11. Lei, X.; Liao, Y.; Liao, Q. Simulation of seed motion in seed feeding device with DEM-CFD coupling approach for rapeseed and wheat. *Comput. Electron. Agric.* **2016**, *131*, 29–39. [CrossRef]
12. Huang, Z.; Li, T.; Yu, Z.; Zhu, C.; Zhao, C. Simulation and experiment of gas-solid two-phase flows in separation chamber of air-screening machine for vegetable seeds. *Trans. Chin. Soc. Agric. Mach.* **2016**, *47*, 70–76. [CrossRef]
13. Li, Y.; Liu, R.; Liu, C.; Liu, L. Simulation and test of seed velocity coupling in seed tube of pneumutic seed metering device. *Trans. Chin. Soc. Agric. Mach.* **2021**, *52*, 54–61+133. [CrossRef]
14. Liu, R.; Liu, Z.; Zhao, J.; Lu, Q.; Liu, L.; Li, Y. Optimization and Experiment of a Disturbance-Assisted Seed Filling High-Speed Vacuum Seed-Metering Device Based on DEM-CFD. *Agriculture* **2022**, *12*, 1304. [CrossRef]
15. Han, D.D.; Zhang, D.X.; Jing, H.R.; Yang, L.; Cui, T.; Ding, Y.Q.; Wang, Z.D.; Wang, Y.X.; Zhang, T.L. DEM-CFD coupling simulation and optimization of an inside-filling air-blowing maize precision seed-metering device. *Comput. Elec. Agri.* **2018**, *150*, 426–438. [CrossRef]
16. Cho, N.; Martin, C.D.; Sego, D.C. A clumped particle model for rock. *Int. J. Rock Mech. Min.* **2007**, *44*, 997–1010. [CrossRef]
17. Potyondy, D.O.; Cundall, P.A. A bonded-particle model for rock. *Int. J. Rock Mech. Min.* **2004**, *41*, 1329–1364. [CrossRef]
18. Chen, Z.; Wang, G.; Xue, D. An approach to calibration of BPM bonding parameters for iron ore. *Powder Technol.* **2021**, *381*, 245–254. [CrossRef]
19. Su, Y.; Xu, Y.; Cui, T.; Gao, X.; Xia, G.; Li, Y.; Qiao, M. Determination and interpretation of bonded-particle model parameters for simulation of maize kernels. *Biosyst. Eng.* **2021**, *210*, 193–205. [CrossRef]
20. Höhner, D.; Wirtz, S.; Kruggel-Emden, H.; Scherer, V. Comparison of the multi-sphere and polyhedral approach to simulate non-spherical particles within the discrete element method: Influence on temporal force evolution for multiple contacts. *Powder Technol.* **2011**, *208*, 643–656. [CrossRef]
21. Markauskas, D.; Kačianauskas, R.; Džiugys, A.; Navakas, R. Investigation of adequacy of multi-sphere approximation of elliptical particles for DEM simulations. *Granul. Matter.* **2010**, *12*, 107–123. [CrossRef]
22. Kodam, M.; Bharadwaj, R.; Curtis, J.; Hancock, B.; Wassgren, C. Cylindrical object contact detection for use in discrete element method simulations, part II—Experimental validation. *Chem. Eng. Sci.* **2010**, *65*, 5863–5871. [CrossRef]

23. Zhou, L.; Yu, J.; Liang, L.; Yu, Y.; Yan, D.; Sun, K.; Wang, Y. Study on key issues in the modelling of maize seeds based on the multi-sphere method. *Powder Technol.* **2021**, *394*, 791–812. [CrossRef]
24. Zhou, L.; Yu, J.; Wang, Y.; Yan, D.; Yu, Y. A study on the modelling method of maize-seed particles based on the discrete element method. *Powder Technol.* **2020**, *374*, 353–376. [CrossRef]
25. Xu, T.; Yu, J.; Yu, Y.; Wang, Y. A modelling and verification approach for soybean seed particles using the discrete element method. Adv. *Powder Technol.* **2018**, *29*, 3274–3290. [CrossRef]
26. Hoshishima, C.; Ohsaki, S.; Nakamura, H.; Watano, S. Parameter calibration of discrete element method modelling for cohesive and non-spherical particles of powder. *Powder Technol.* **2021**, *386*, 199–208. [CrossRef]
27. Mellmann, J. The transverse motion of solids in rotating cylinders—Forms of motion and transition behavior. *Powder Technol.* **2001**, *118*, 251–270. [CrossRef]
28. Liu, J.; Wang, M.; Wang, X.; Yao, L.; Yang, M.; Yue, Q. Research on particle swarm collision search and advancement algorithm for CFD-DEM coupling domain solving. *Chin. J. Theor. Appl. Mech.* **2021**, *53*, 1569–1585. [CrossRef]
29. Nguyen, D.; Rasmuson, A.; Björn, I.N.; Thalberg, K. CFD simulation of transient particle mixing in a high shear mixer. *Powder Technol.* **2014**, *258*, 324–330. [CrossRef]
30. Bao, Y.; Li, T.; Wang, D.; Cai, Z.; Gao, Z. Discrete element method study of effects of the impeller configuration and operating conditions on particle mixing in a cylindrical mixer. *Particuology* **2020**, *49*, 146–158. [CrossRef]
31. Xu, J.; Wang, X.; Zhang, Z.; Wu, W. Discrete Element Modeling and Simulation of Soybean Seed Using Multi-Spheres and Super-Ellipsoids. *IEEE Access* **2020**, *8*, 222672–222683. [CrossRef]
32. Govender, N.; Wilke, D.N.; Wu, C.Y.; Rajamani, R.; Khinast, J.; Glasser, B.J. Large-scale GPU based DEM modeling of mixing using irregularly shaped particles. *Adv. Powder Technol.* **2018**, *29*, 2476–2490. [CrossRef]
33. Xu, J.; Sun, S.; He, Z.; Wang, X.; Zeng, Z.; Li, J.; Wu, W. Design and optimisation of seed-metering plate of air-suction vegetable seed-metering device based on DEM-CFD. *Biosyst. Eng.* **2023**, *230*, 277–300. [CrossRef]